Journal of Electroanalytical Chemistry 688 (2013) 143–150

Contents lists available at SciVerse ScienceDirect

Journal of Electroanalytical Chemistry

journal homepage: www.elsevier.com/locate/jelechem

Platinum nanoparticles functionalized with acetylene derivatives: Electronic conductivity and electrocatalytic activity in oxygen reduction

Ke Liu [a], Xiongwu Kang [a], Zhi-You Zhou [b], Yang Song [a], Lyman J. Lee [a], Daniel Tian [a], Shaowei Chen [a,*]

[a] Department of Chemistry and Biochemistry, University of California, 1156 High Street, Santa Cruz, CA 95064, USA
[b] State Key Laboratory of Physical Chemistry of Solid Surfaces, Department of Chemistry, College of Chemistry and Chemical Engineering, Xiamen University, Xiamen, Fujian 361005, PR China

ARTICLE INFO

Article history:
Available online 24 July 2012

Keywords:
Platinum nanoparticle
Acetylene
Electronic conductivity
Oxygen reduction reaction
Intraparticle charge delocalization

ABSTRACT

Stable platinum nanoparticles were prepared by the self assembly of acetylene derivatives (1-alkynes, 4-ethylphenylacetylene, and 4-tert-butylphenylacetylene) onto bare Pt colloid surfaces. Transmission electron microscopic measurements showed that the nanoparticles exhibited an average core size of 2.85 ± 0.62 nm. FTIR study showed that with the acetylene ligands adsorbed onto the Pt nanoparticle surface, the ≡C—H vibrational stretches disappeared completely, along with a substantial redshift of the C≡C vibrational stretch, as compared to those of the monomeric ligands. These were ascribed to the breaking of the ≡C—H bond and the formation of $Pt_{surface}$—H and $Pt_{surface}$—C≡ at the metal–ligand interface. The conjugated bonding interactions between the triple bond and Pt were found to lead to extensive intraparticle charge delocalization between the acetylene moieties, and hence unique photoluminescence properties of the nanoparticles. For nanoparticles functionalized with 4-ethylphenylacetylene or 4-tert-butylphenylacetylene, the excitation and emission peak positions showed an apparent redshift as compared to those of 1-alkyne-capped platinum nanoparticles. Electronic conductivity measurements of the nanoparticle solids showed that for the nanoparticles capped with 1-alkynes or 4-ethylphenylacetylene, the temperature dependence of the ensemble conductivity was consistent with that of semiconducting materials, whereas for the 4-tert-butylphenylacetylene-capped nanoparticles, metallic behaviors were observed instead. An apparent discrepancy was also observed in the electrocatalytic reduction of oxygen in alkaline media, where the specific activity was all markedly better than that of commercial Pt/C catalysts, with the best performance by the 4-ethyphenylacetylene-capped Pt nanoparticles. These observations were accounted for by the deliberate manipulation of the electronic structure of the Pt nanoparticles by the organic ligands.

1. Introduction

Recent studies have shown that the material properties of organically capped transition-metal nanoparticles can be readily manipulated not only by the chemical nature of the metal cores and protecting ligands but also by the metal–ligand interfacial bonding interactions [1]. For instance, when metal nanoparticles are stabilized by metal–carbon covalent bonds, the resulting nanoparticles exhibit much enhanced electronic conductivity of the solid ensembles as compared to the mercapto-stabilized counterparts, which is accounted for by the reduced metal–ligand interfacial contact resistance and hence the extensive spilling of core electrons into the organic capping matrix that facilitated interparticle charge transfer [2,3]. In addition, when the ligands are bound onto the nanoparticle surface by conjugated chemical linkages, effective intraparticle charge delocalization may occur for the particle-bound functional moieties, leading to the emergence of unprecedented optical and electronic properties that are analogous to those of their dimeric forms. This has been manifested in ruthenium nanoparticles functionalized with carbene fragments, alkynides, as well as acetylene derivatives using electroactive species such as ferrocene and fluorophores such as anthracene and pyrene as the molecular probes [4–10].

In more recent studies, we found that by deliberate chemical functionalization of Pd and Pt nanoparticles with selected aliphatic fragments using diazonium salts as the precursors (with the formation of M—C bonds), the resulting nanoparticles exhibited significant enhancement of their electrocatalytic activities in formic acid oxidation as well as oxygen reduction [11–13]. The somewhat unexpected behaviors were accounted for by the unique tuning of the electronic structures of the metal cores that impacted the bonding interactions with the respective reactants. Yet, the effects of other metal–ligand interfacial bonding interactions on the

* Corresponding author.
E-mail address: shaowei@ucsc.edu (S. Chen).

1572-6657/$ - see front matter © 2012 Elsevier B.V. All rights reserved.
http://dx.doi.org/10.1016/j.jelechem.2012.07.009

nanoparticle electrocatalytic activity remain largely unexplored. This is the primary motivation of the present study.

In this study, we prepared a series of platinum nanoparticles that were capped by the self-assembly of acetylene derivatives, ranging from straight-chain 1-alkynes to aromatic acetylene derivatives. In our previous study with ruthenium nanoparticles, we demonstrated that terminal alkynes adsorbed onto the nanoparticle surface forming ruthenium–vinylidene (Ru=C=CH—) interfacial bonds by virtue of a tautomeric rearrangement process [10]. Similar self-assembly was observed with Pt nanoparticles. The bonding interactions between the acetylene derivatives with Pt were then examined by FTIR, UV–vis and photoluminescence spectroscopic measurements. The results suggested effective breaking of the ≡C—H bond and the formation of $Pt_{surface}$—H and $Pt_{surface}$—C≡ at the metal–ligand interface. With such conjugated metal–ligand bonding interactions, the resulting nanoparticles exhibited interesting electronic conductivity properties. For Pt nanoparticles functionalized with 1-alkynes or 4-ethylphenylacetylene, temperature dependence of the ensemble electronic conductivity was consistent with that of semiconducting materials, whereas for 4-tert-butylphenylacetylene-capped nanoparticles, metallic behaviors were observed instead. This discrepancy of the ensemble conductivity properties also led to an apparent variation of the electrocatalytic activity in oxygen reduction. On the basis of onset potential and kinetic current density, the 4-ethylphenylacetylene-capped nanoparticles were found to exhibit the best performance among the series. This was accounted for by the combined contributions of (i) effective partial removal of nanoparticle surface ligands for ready accessibility of the nanoparticle surface by oxygen and electrolyte counter ions and (ii) tuning of the nanoparticle electronic structures that impacted the bonding interactions with oxygen. These results further demonstrate that surface chemical functionalization may represent a unique and effective tool in the manipulation and optimization of their electrocatalytic activity.

2. Experimental section

2.1. Chemicals

Platinum chloride ($PtCl_2$, 98 %, Alfa Aesar), 1-decyne (HC10, TCI America), 1-dodecyne (HC12, ACROS, 98%), 1-tetradecyne (HC14, Wako), 1-hexadecyne (HC16, Alfa Aesar, 90%), 4-ethylphenylacetylene (EPA, 99%, Fisher Scientific), and 4-tert-butylphenylacetylene (BPA, 90+%, Fisher Scientific), 1,2-propanediol (ACROS), and sodium acetate trihydrate ($NaOAc{\cdot}3H_2O$, MC&B) were used as received. A commercial Pt/C catalyst was purchased from Alfa Aesar (20 wt.%, HiSPEC^{TM}3000, Johnson Matthey). All solvents were obtained from typical commercial sources and used without further treatment. Water was supplied by a Barnstead Nanopure water system (18.3 MΩ cm).

2.2. Preparation of platinum nanoparticles

Pt nanoparticles stabilized by acetylene derivatives were prepared by adopting a previous procedure for the synthesis of alkyne-capped ruthenium nanoparticles [10]. Briefly, in a typical reaction, 0.28 mmol of $PtCl_2$ was dissolved in 2 mL of concentrated HCl and heated at 60 °C for 30 min, into which $NaHCO_3$ was added until no bubbling was observed. The resulting Na_2PtCl_4 and 2 mmol of NaOAc were then mixed in 200 mL of 1,2-propanediol and the solution was heated to 165 °C for 1 h under vigorous stirring. The solution turned dark brown signifying the formation of nanometer-sized platinum colloids. Upon cooling to room temperature, the solution was split equally into six round-bottom flasks into which a calculated amount of an acetylene derivative dissolved in toluene was added. The self-assembly of the ligands onto the platinum surface led to the effective extraction of the nanoparticles into the toluene phase, as manifested by the color appearance. The toluene part was collected, dried with a rotary evaporator and rinsed extensively with ethanol to remove excessive ligands. For alkyne-capped nanoparticles, they were denoted as PtHC*x* with *x* being the number of carbon atoms in the corresponding monomeric alkyne ligands; and for those stabilized by 4-ethylphenylacetylene and 4-tert-butylphenylacetylene, they were referred to as PtEPA and PtBPA, respectively.

2.3. Spectroscopy

The morphology and size of the Pt nanoparticles were characterized by transmission electron microscopy studies (TEM, Philips CM300 at 300 kV). More than 300 nanoparticles were measured to obtain a size histogram. ^{1}H NMR spectroscopic measurements were carried out by using concentrated solutions of the nanoparticles in $CDCl_3$ with a Varian Unity 500 MHz NMR spectrometer. The absence of any sharp features indicated that the nanoparticles were free of excessive unbound ligands. UV–vis spectroscopic studies were performed with an ATI Unicam UV4 spectrometer using a 1 cm quartz cuvette with a resolution of 2 nm. Photoluminescence characteristics were examined with a PTI fluorospectrometer. FTIR measurements were carried out with a Perkin–Elmer FTIR spectrometer (Spectrum One, spectral resolution 4 cm^{-1}), where the samples were prepared by casting the particle solutions onto a KBr disk.

2.4. Electronic conductivity

Electronic conductivity of solid films of the platinum nanoparticles was evaluated by using a procedure detailed previously [10]. A particle film was formed by dropcasting 1 μL of a concentrated particle solution in toluene (60 mg/mL) onto an interdigitated array (IDA) electrode (25 pairs of gold fingers of 3 mm × 5 μm × 5 μm, from ABTECH). At least 30 min was allowed for solvent evaporation, and the film thickness was found to be greater than the height of the IDA fingers. Conductivity measurements were then carried out in vacuum (Cryogenic Equipment, JANIS CO) with a CHI710 Electrochemical Workstation at different temperatures (Lakeshore 331 Temperature Controller). The ensemble conductivity (σ) was evaluated by the equation $\sigma = \left(\frac{1}{49R}\right)\left(\frac{L}{S}\right)$, where R is the ensemble resistance calculated from the slope of the I–V curves, L is the IDA electrode interfinger gap (5 μm) and S is the film cross-section area approximated by (finger height, 5 μm) × (finger length, 3 mm). The constant (49) reflects that there are totally 49 junctions which are in parallel within the IDA chip.

2.5. Electrochemistry

Electrochemical tests were carried out in a standard three-electrode cell connected to a CHI 710C electrochemical work station, with a Pt foil counter electrode and a Hg/HgO reference electrode in a 0.1 M NaOH solution (from CH Instruments). The working electrode is a rotating gold ring – glassy-carbon disk electrode (RRDE). To prepare catalyst solutions for oxygen reduction tests, dilute solutions of the Pt nanoparticles in toluene were mixed with XC-72 carbon black and a Nafion 117 solution (5 wt.%, Fluka) to form a well dispersed catalyst "ink" (Pt:carbon black = 1:4 (w/w), Nafion: 0.05%) under ultrasound. A calculated amount of the catalyst inks was slowly dropcast onto the RRDE. As soon as the electrode was dried, a dilute Nafion solution (0.1 wt.%, 3 μL) was added onto it. The Pt loading was 2.44 μg for PtHC10, 1.90 μg for PtEPA, 1.90 μg for PtBPA, and 2.00 μg for commercial Pt/C.

3. Results and discussion

3.1. Structural characterizations

Fig. 1 depicts a representative TEM micrograph of the Pt nanoparticles. It can be seen that the nanoparticles were well dispered without apparent aggregation, suggesting effective passivation of the nanoparticles by the self-assembly of acetylene derivatives onto the Pt surface, and the resulting nanoparticles exhibited well-defined crystalline structures. From the TEM image, one can see that the lattice fringes display a spacing of 0.230 nm corresponding to the separation between the Pt(111) planes. Furthermore, it can be seen that the size of the nanoparticles was rather uniform. In fact, the nanoparticle core size histogram based on a statistical analysis of more than 300 nanoparticles (figure inset) shows that the nanoparticles exhibited an avergae core size of 2.85 ± 0.62 nm.

The structures of the capping ligands were then examined by FTIR measurements, as depicted in Fig. 2 with PtHC10, PtEPA and PtBPA nanoparticles. The spectra of PtHC12, PtHC14, and PtHC16 nanoparticles were similar to that of PtHC10 and hence not shown. Whereas the monomeric ligands (dashed curves) all exhibited a well-defined ≡C—H vibrational stretch (3314 cm^{-1} for HC10, and 3294 cm^{-1} for both EPA and BPA), such a feature vanished completely with the nanoparticle samples (solid curves), indicating facile breaking of the ≡C—H bond when the ligands were adsorbed onto the nanoparticle surface. Previously Muetteries et al. [14] carried out an ultra-high vacuum study of the chemical reactivity of acetylene on Pt{111} and Pt{100} surfaces and found that at ambient temperature the carbon-hydrogen bond breaking was absent on the Pt{111} surface, whereas the process was detectable for Pt{100} even at 20 °C with the formation of $Pt_{surface}$—H and $Pt_{surface}$—C≡ bonds. For the nanoparticles prepared above, the fact that the lattice fringes are well defined for the Pt(111) planes (Fig. 1) suggests that the {100} facets might constitute a substantial fraction of the metal core surface, which facilitated the breaking of the ≡C—H bond when the acetylene derivatives were

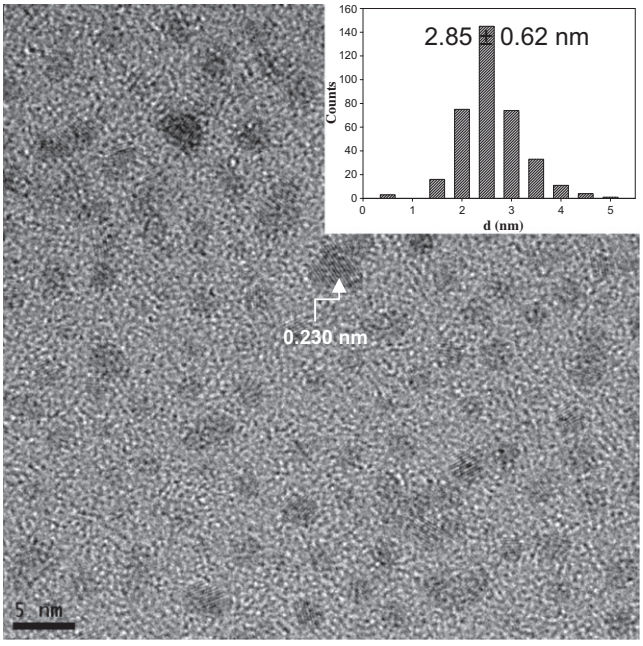

Fig. 1. Representative TEM micrograph of PtHC10 nanoparticles prepared by thermolytic reduction of $PtCl_2$. Scale bar 5 nm. Inset shows the corresponding nanoparticle core size histogram.

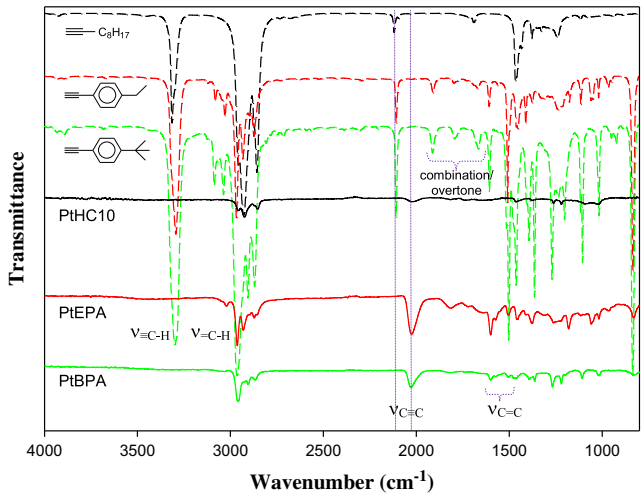

Fig. 2. FTIR spectra of PtHC10, PtEPA, and PtBPA nanoparticles along with those of monomeric HC10, EPA and BPA ligands.

adsorbed onto the Pt surfaces. Similar behaviors were observed with alkyne-capped ruthenium nanoparticles [10], where the tautomeric rearrangement of the acetylene moieties adsorbed on the Ru nanoparticle surface led to a dynamic equilibrium between the η^2 configuration and a Ru–vinylidene interfacial linkage with the corresponding metal hydride as the intermediate species. Notably, the disappearance of the ≡C—H vibrational stretches also indicates that the platinum nanoparticles were free of excessive unbound ligands.

Additionally, for EPA and BPA monomers, the spectral features of the ring skeleton vibrations (C=C) at 1609 and 1460 cm^{-1} and C—H deformation at 841 cm^{-1} are also well-defined, along with the combination and/or overtone of the ring deformations that emerged between 1630 and 1970 cm^{-1} and the ring C—H vibrations at 3042 and 3089 cm^{-1} [15]. These characteristics are also very well-defined with the PtEPA and PtBPA nanoparticles.

The breaking of the ≡C—H bond and the formation of the Pt—C≡ linkage also led to a drastic variation of the C≡C vibrational stretch. From Fig. 2, it can be seen that, for the monomeric ligands (dashed curves), the C≡C vibrational stretch can be identified at 2122 cm^{-1} for HC10, and 2110 cm^{-1} for both EPA and BPA; whereas when the ligands were bound onto the nanoparticle surface, the C≡C vibrational stretch appears at a much lower wavenumber position, 2020 cm^{-1} for PtHC10, and 2030 cm^{-1} for PtEPA and PtBPA. This observation strongly indicates that the ligands were indeed chemically bonded onto the Pt surface, and the decreasing bonding order (lower peak wavenumber) might be attributed to the $\sigma\pi$ bonding interactions between the triple-bond moieties and the platinum metal cores, where effective intraparticle charge delocalization occurred between the particle-bound acetylene moieties. In fact, such a phenomenon has been observed extensively with other nanoparticles passivated by conjugated metal–ligand bonding interactions [7,10,16].

Notably, the fact that only one peak was observed for the C≡C vibrational stretch with the Pt nanoparticles prepared above is also consistent with the formation of $Pt_{surface}$—H and $Pt_{surface}$—C≡ bonds at the metal–ligand interface. Note that for alknyide-capped Ru nanoparticles [7], also one peak was observed for the particle-bound C≡C bonds (i.e., with $Ru_{surface}$—C≡ interfacial bonds). However, the behaviors were sharply different with alkyne-capped ruthenium nanoparticles [10] or with alkynes adsorbed onto Au and Ag surfaces by surface-enhanced Raman scattering (SERS) measurements [17], where three peaks emerged at *ca.* 2056 cm^{-1}, 1976 cm^{-1}, and 1950 cm^{-1} for the C≡C vibrational

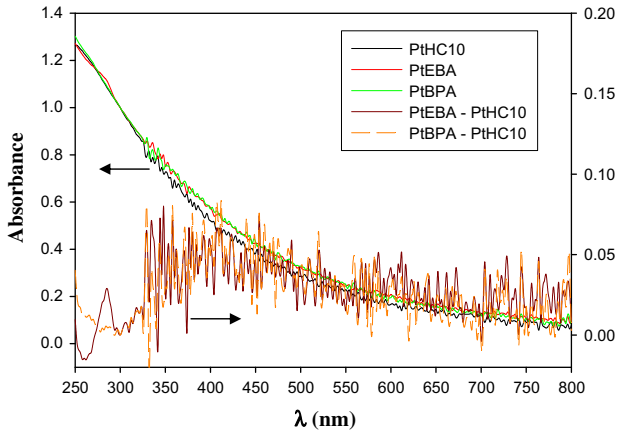

Fig. 3. UV–vis spectra of PtHC10, PtEBA, and PtBPA nanoparticles in $CHCl_3$. Note that the spectra have been normalized to their respective absorbance at 300 nm. The difference spectra between the PtEPA (PtBPA) and PtHC10 nanoparticles are also included in the figure (right axis).

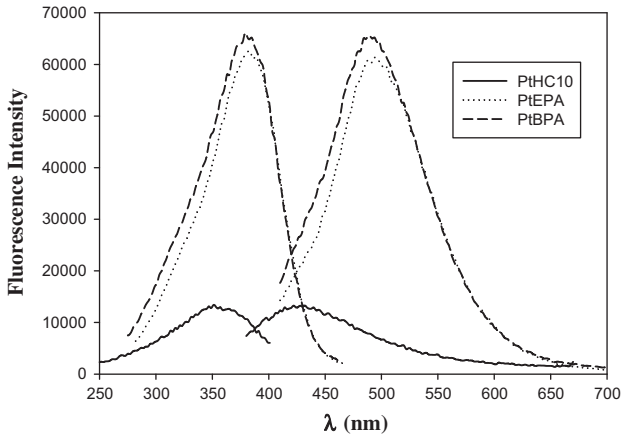

Fig. 4. Excitation and emission spectra of PtHC10 (solid curves), PtEPA (dotted curve) and PtBPA (dashed curve) in $CHCl_3$. Note that the fluorescence intensity has been normalized to the optical density at the respective excitation wavelength position.

stretch, because of the formation of metal–vinylidene (Ru═C═CH─) linkages that display symmetric and asymmetric vibrational modes.

With the formation of $Pt_{surface}$─C≡ bonds at the metal–ligand interface, the Pt nanoparticles exhibited unique optical characteristics [7]. Fig. 3 depicts the UV–vis absorption spectra of PtHC10 (black curve), PtEPA (red[1] curve), and PtBPA (green curve) nanoparticles in $CHCl_3$. Note that the spectra have been normalized to their respective absorbance at 300 nm. It can be seen that all featured an exponential decay profile (the co-called Mie scattering), as anticipated for nanometer-sized transition-metal particles [18]. In comparison with PtHC10 nanoparticles, both PtEPA and PtBPA nanoparticles exhibited an additional broad absorption peak within the range of 300 and 550 nm (centered around 400 nm, brown and orange curves), as manifested in the difference spectra in the figure. This is likely due to intraparticle charge delocalization that was further extended by the participation of the phenyl π electrons [10]. In fact, because of the extended conjugation, the particle-bound phenylacetylene moieties in PtEPA and PtBPA nanoparticles now behaved analogously to diphenyldiacetylene (Ph─C≡C─C≡C─Ph) [19]. The resulting nanoparticles also exhibited interesting photoluminescence characteristics that are consistent with those of diphenyldiacetylene derivatives, as detailed below.

Fig. 4 depicts the excitation and emission spectra of the PtHC10 (solid curves), PtEPA (dotted curves), and PtBPA (dashed curves) nanoparticles in $CHCl_3$. Note that the fluorescence intensity has been normalized to the optical density at the respective excitation wavelength position. It can be seen that for Pt nanoparticles capped with 1-decyne (and other 1-alkynes), the excitation (λ_{ex}) and emission (λ_{em}) peak positions can be identified at 352 nm and 430 nm, respectively, consistent with the results of our previous studies with ruthenium nanoparticles capped with 1-alkynes [10] or alkynide derivatives derivatives [7]. Yet, for the nanoparticles functionalized with aromatic derivatives of acetylene, λ_{ex} and λ_{em} exhibit a significant redshift to 382 nm and 492 nm, respectively, for both PtEPA and PtBPA nanoparticles. This is most probably due to the additional contribution of the phenyl π electrons to the conjugation between the particle-bound acetylene moieties [19,20], which may also account for the (normalized) fluorescence intensity of both PtEPA and PtBPA nanoparticles that is over five times greater than that of PtHC10, as depicted in Fig. 4.

[1] For interpretation of color in Figs. 2,3,5,6, and 8, the reader is referred to the web version of this article.

3.2. Electronic conductivity

The Pt nanoparticles obtained above also exhibited interesting electronic properties, as reflected in the electronic conductivity measurements of the nanoparticle solid films. Fig. 5 depicts the current–potential (I–V) curves of (A) PtHC10, (B) PtEPA and (C) PtBPA nanoparticle films prepared by dropcasting 1 μL of a 60 mg/mL particle solution in toluene onto an IDA surface. Within the bias voltage of −0.80 to +0.80 V, obvious ohmic behaviors (linear I–V responses) were observed throughout the entire temperature range of 80–300 K, signifying very efficient interparticle charge transfer, which might be, at least in part, attributed to the conjugated metal–ligand interfacial bonding interactions that allows extensive spilling of the metal core electrons into the organic ligand matrix [10]. Furthermore, it can be seen that the conductivity of the nanoparticle solid films was markedly greater with PtBPA and PtEPA than that of PtHC10. For instance, at 300 K, the ensemble conductivity was 74.1 mS/m, 0.14 mS/m, and 0.051 mS/m for the PtBPA, PtEPA, and PtHC10 nanoparticles, respectively, consistent with the reduced charge transfer resistance of the aromatic spacers as compared with that of the saturated counterparts, which has been observed extensively in prior studies [21]. Note that the conductivity of these nanoparticles ensemble films is about 8–11 orders of magnitude lower than that of metallic platinum (9.52×10^6 S/m at 293 K) [22], as a result of the metal–organic hybrid nature of the nanoparticles.

More interestingly, the three nanoparticles exhibited a significantly different variation of the ensemble conductivity with temperature. For (A) PtHC10 and (B) PtEPA nanoparticles, the ensemble conductivity increased monotonically with increasing temperature from 80 to 300 K, indicating semiconducting characteristics of the nanoparticle solid films which is consistent with the composite nature of the nanoparticle materials. Such a behavior has also been observed previously with a number of organically capped metal nanoparticles, where interparticle charge transfer was accounted for by a thermally activated hopping mechanism between adjacent nanoparticles [2,3]. From the temperature dependence of the ensemble conductivity (Fig. 6), the activation energy for interparticle charge transfer can be estimated, which is ca. 76.3 meV and 46.3 meV for the PtHC10 and PtEPA nanoparticles, respectively. Note that for ruthenium nanoparticles functionalized by 1-alkynes of varied chain lengths, the activation energy for interparticle charge transfer was also found to be around 70 meV [10]. The reduced activation energy for PtEPA, as compared

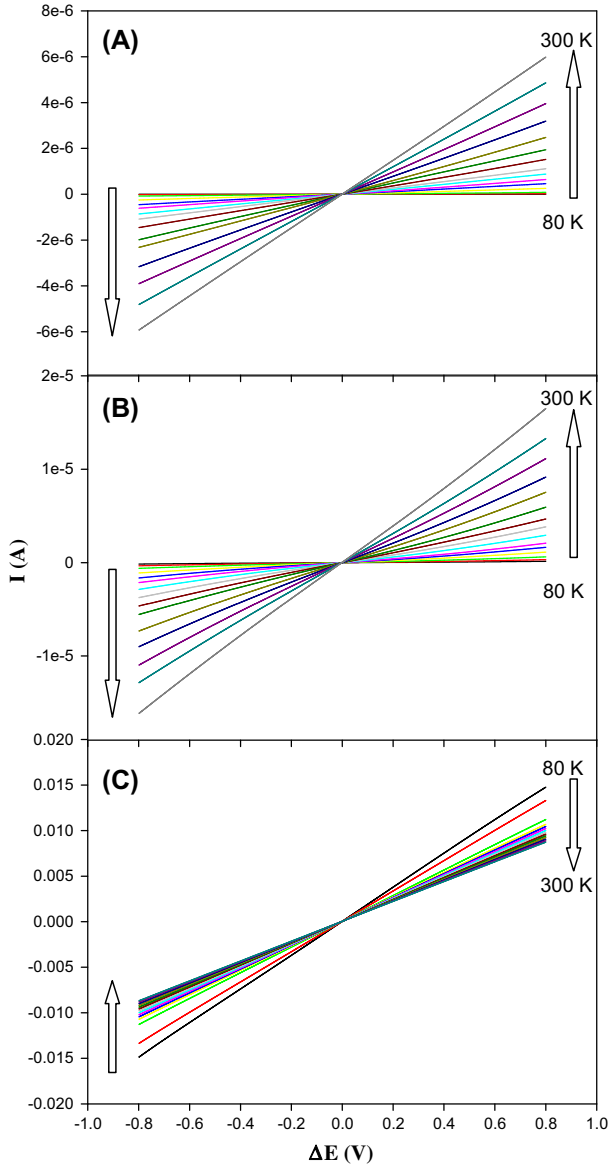

Fig. 5. Current–potential (*I–V*) curves of the nanoparticle solid ensembles at varied temperatures: (A) PtHC10, (B) PtEPA, and (C) PtBPA. Potential scan rate 20 mV/s. Arrows denote the increase of temperature from 80 K to 300 K.

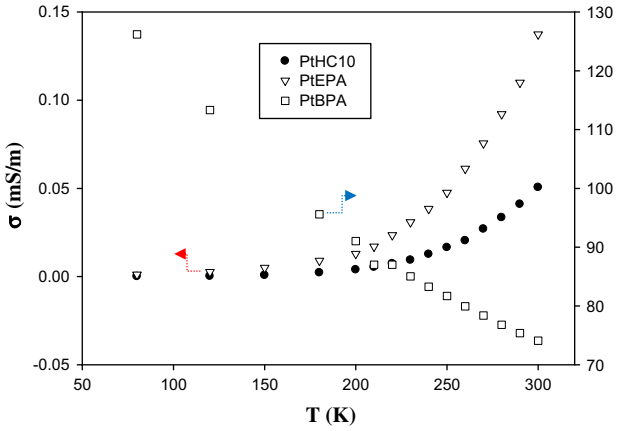

Fig. 6. Variation of nanoparticle ensemble conductivity with temperature. Data are obtained from the slopes of the *I–V* curves in Fig. 5. The left *y* axis is for both PtHC10 and PtEPA, and the right *y* axis for PtBPA alone.

to that of PtHC10, is most likely due to the lower charge transfer resistance of the aromatic moiety than with the saturated aliphatic chain.

However, for the PtBPA nanoparticles (Fig. 5C), the temperature dependence of the ensemble conductivity was totally different. As depicted in Fig. 6, the nanoparticle electronic conductivity actually decreased with increasing temperature, a behavior typically anticipated with metallic materials [22]. In a previous study with biphenyl-functionalized palladium and titanium nanoparticles [2,3], we observed similar metallic characters in conductivity measurements, which was ascribed to the M—C covalent bonding interactions that reduced the contact resistance at the metal–ligand interface [23–25] as well as the $\pi-\pi$ stacking between ligands of adjacent particles in the solid films, as a result of ligand intercalations that serves as an effective pathway for interparticle charge transfer [26]. Similar behaviors were also observed with ruthenium nanoparticles passivated by varied aliphatic fragments with Ru—C bonding interactions as a result of the strong metal–ligand interfacial bonding interactions [3]. In the present study, with the conjugated Pt—C≡ interfacial linkage, the metal–ligand contact resistance is anticipated to be low, leading to extended conjugation between the particle-bound phenylacetylene moieties (e.g., as manifested in the photoluminescence measurements in Figs. 3 and 4) and hence a reduced energetic barrier for interparticle charge transfer.

Additional contributions may arise from the tert-butyl substituent group. Note that in nanoparticle solids, interparticle charge transfer takes place by a percolation pathway as the conducting metallic cores are embedded within an organic matrix. For straight-chain aliphatic capping ligands, because of the tight packing on the nanoparticle surface, charge transfer between neighboring nanoparticles most probably occurs by a hopping process through the molecular ligands, and the ensemble conductivity decreases exponentially with the ligand chain length because of intercalation between ligands of neighboring particles. In fact, this was manifested in further studies with the same Pt nanoparticles but capped with 1-alkynes of different chain lengths (i.e., 1-dodecyne, 1-tetradecyne, and 1-hexadecyne; results not shown), similar to that observed with alkyne-capped ruthenium nanoparticles [10]. In contrast, for aromatic ligands, the packing is generally less tight because of steric hindrance, in particular with branched substituents such as the tert-butyl group. Thus, in these nanoparticle solid films, interparticle charge transfer is not necessarily through the surface ligands, but rather, via surface defects. Such a process is likely facilitated by the tert-butyl moiety, as tert-butyl group is known to exhibit higher electron-donating capability than the ethyl one [27]. This may explain why the PtEPA nanoparticles did not display the metallic characters like PtBPA, despite a similar ligand structure and extended chain length. Such tert-butyl effects have also been observed with molecular systems. For instance, recently Hankache and Wenger [28] examined the photoinduced electron transfer of covalent ruthenium(bipyridine) – anthraquinone dyads and observed that the introduction of electron-donating tert-butyl substituents into the bipyridine ligands led to an order of magnitude enhancement of the electron transfer rate.

3.3. Electrocatalytic activity

In addition to an apparent difference of the ensemble conductivity, the above Pt nanoparticles also showed a marked variation of their electrocatalytic behaviors in oxygen reduction. Fig. 7 shows the steady-state cyclic voltammograms of a glassy-carbon disk electrode modified with a same amount (~2 μg) of PtHC10 (solid curve), PtEPA (dotted curve), PtBPA (dashed curve) and commercial Pt/C (dashed-double dotted curve) nanoparticles in 0.1 M NaOH at a potential sweep rate of 100 mV/s, after the electrodes were

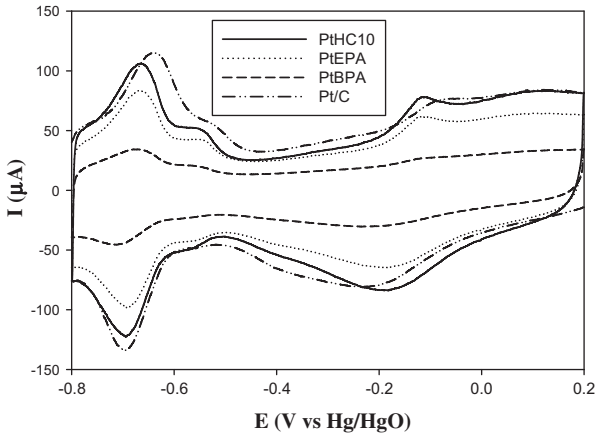

Fig. 7. Cyclic voltammograms of a glassy-carbon disk electrode modified with PtHC10, PtEPA, Pt-BPA and commercial Pt/C nanoparticles in a nitrogen-purged 0.1 M NaOH solution. Pt loadings were 2.44 μg (PtHC10), 1.90 μg (PtEPA), 1.90 μg (PtBPA), and 2.00 μg (Pt/C). Potential scan rate 100 mV/s.

subject to about 30 potential cycles within the potential range of −0.80 V and +0.20 V (vs Hg/HgO). It can be seen that at all electrodes, the platinum butterfly features are quite well-defined. That is, in the anodic scan, a voltammetric peak emerged at ca. −0.11 V which can be attributed to the oxidation of the Pt surface. This was then reduced in the cathodic scan with a peak at −0.19 V. In addition, there appear a pair of voltammetric waves within the potential range of −0.50 V and −0.80 V, which may be ascribed to hydrogen adsorption/desorption on (naked) Pt surfaces, and from the integrated peak areas, the effective electrochemical surface area of the electrode was estimated to be 22.8 m^2/g_{Pt} (PtHC10), 21.0 m^2/g_{Pt} (PtEPA), and 8.1 m^2/g_{Pt} (PtBPA). In comparison to the physical surface area based on the nanoparticle average core size (98.1 m^2/g_{Pt} from Fig. 1), this represents 23.2%, 21.4%, and 8.3% of the Pt nanoparticle surface that was made accessible to electrolyte ions by the electrochemical treatments. Note that for "bare" commercial Pt/C, the effective electrochemical surface area was markedly higher at 61.5 m^2/g_{Pt}, signifying that about 72.5% of the Pt nanoparticle surface was electrochemically accessible [13].

Interestingly, the effective desorption of the capping ligands from the Pt nanoparticle surface happened to follow a trend opposite of the nanoparticle ensemble conductivity (vide ante). For the PtHC10 and PtEPA nanoparticles, both showed that more than 20% of the Pt surface area became accessible after the electrochemical treatments, whereas only 8.3% of the PtBPA nanoparticle surface was exposed. Note that the PtBPA nanoparticles exhibited metallic characters in interparticle charge transfer (Fig. 6), and thus the high electronic conductivity dictates that the potential drop within the nanoparticle layer would be significantly smaller than that in the semiconducting PtHC10 and PtEPA nanoparticles. Thus, the electrochemical desorption of the capping ligands from the PtBPA nanoparticle surface was less effective.

This discrepancy of the electrochemical reactivity also led to an apparent difference in the electrocatalytic reduction of oxygen, an important reaction process in fuel cell electrochemistry. Fig. 8 shows the ring and disk voltammograms of a gold ring – glassy-carbon disk electrode with the disk modified with (A) PtHC10, (B) PtEPA, (C) PtBPA, and (D) commercial Pt/C nanoparticles in an oxygen-saturated 0.1 M NaOH solution at varied rotation rates (the electrodes were the same as those in Fig. 7). It can be seen that on the disk electrode the cathodic currents of oxygen reduction start to emerge at ~+0.067 V (PtHC10), +0.077 V (PtEPA), +0.046 V (PtBPA), and +0.026 V (Pt/C), respectively. That is, the onset potentials of the three acetylene-capped Pt nanoparticles were all somewhat more positive than that at the commercial Pt/C catalysts, implying that oxygen reduction was facilitated at the acetylene-functionalized Pt nanoparticles as compared to the naked ones. Additionally, the voltammetric currents for oxygen reduction reach a plateau at potentials more negative than −0.40 V, and increase with increasing electrode rotation rate (from 100 to 2500 rpm). Notably, the corresponding ring currents collected at +0.40 V are all at least one order of magnitude smaller, indicating that the amounts of hydrogen peroxide (H_2O_2) produced during oxygen reduction were minimal. Importantly, from the ratio between the ring (I_R) and disk (I_D) currents, the number of electron transfer (n) in oxygen electroreduction can be estimated, $n = \frac{4I_D}{I_D + \frac{I_R}{N}}$ with N being the collection efficiency (37%) [13]: PtHC10, 3.98; PtEPA, 3.92; PtBPA, 3.91; and Pt/C, 3.81 [13], suggesting that with the four nanoparticle catalysts, oxygen underwent efficient four-electron reduction to water, $O_2 + 2H_2O + 4e \leftrightarrow 4OH^-$.

Further insights into the electron transfer dynamics of oxygen reduction were obtained from the analysis of the Koutecky–Levich plots (I^{-1} vs $\omega^{-1/2}$). Note that in rotating disk voltammetric measurements, the measured currents (I) may involve both kinetic (I_K) and diffusion (I_D) controlled contributions [29],

$$\frac{1}{I} = \frac{1}{I_K} + \frac{1}{I_D} + = \frac{1}{I_K} + \frac{1}{B\omega^{1/2}} \tag{1a}$$

$$B = 0.62\, nAFC_O D_O^{2/3} \nu^{-16} \tag{1b}$$

$$I_K = nFAkC_O \tag{1c}$$

where ω is the electrode rotation rate, n is the overall number of electron transfer, F is the Faraday constant, C_O is the bulk concentration of O_2 dissolved in the electrolyte, D_O is the diffusion coefficient for O_2, and ν is the kinematic viscosity of the electrolyte [30]. Thus, the plots of I^{-1} versus $\omega^{-1/2}$ are anticipated to yield straight lines with the intercept corresponding to I_K (Eq. (1c)) and the slopes reflecting the so-called B factors (Eq. (1b)). Fig. 9 displays the Koutecky–Levich plots of oxygen electroreduction at the four nanoparticle catalysts. One can see that within the potential range of −0.10 V to −0.30 V, the experimental data can all be fitted very well with linear regressions, and the slopes of each nanoparticle catalyst remained approximately constant. The linearity and parallelism of the plots are usually taken as a strong indication of a first-order reaction with respect to dissolved oxygen.

In addition, from the y-axis intercepts of the linear regressions, the kinetic currents in oxygen reduction can also be quantitatively evaluated (Eq. (1a)). Interestingly, when normalized to the effective electrochemical surface area as estimated from Fig. 7, the kinetic current density (J_K) of the three acetylene-functionalized Pt nanoparticles was all markedly higher than that of the commercial "bare" Pt/C catalysts (Fig. 10), again, suggesting that surface functionalization by acetylene derivatives on the Pt surface facilitated the electroreduction of oxygen. Additionally, one may notice that whereas the experimental data for PtHC10 were somewhat scattered, the kinetic current density of PtEPA was consistently greater than that of PtBPA within the entire potential range of −0.10 V to −0.30 V. For instance, at −0.18 V, the kinetic current densities (J_K) at the four nanoparticle catalysts are 12.6 mA/cm^2 (PtBPA), 19.1 mA/cm^2 (PtEPA), 12.3 mA/cm^2 (PtHC10), and 4.1 mA/cm^2 (Pt/C), respectively.

Therefore, it can be seen that on the basis of the onset potential and kinetic current density, of the three nanoparticle catalysts, the PtEPA nanoparticles exhibited the best electrocatalytic activity for oxygen reduction. This may be accounted for by the reaction mechanism of oxygen reduction on Pt surfaces. It has been known that the first electron-transfer process for the adsorbed oxygen molecules represents the rate-determining step [31,32],

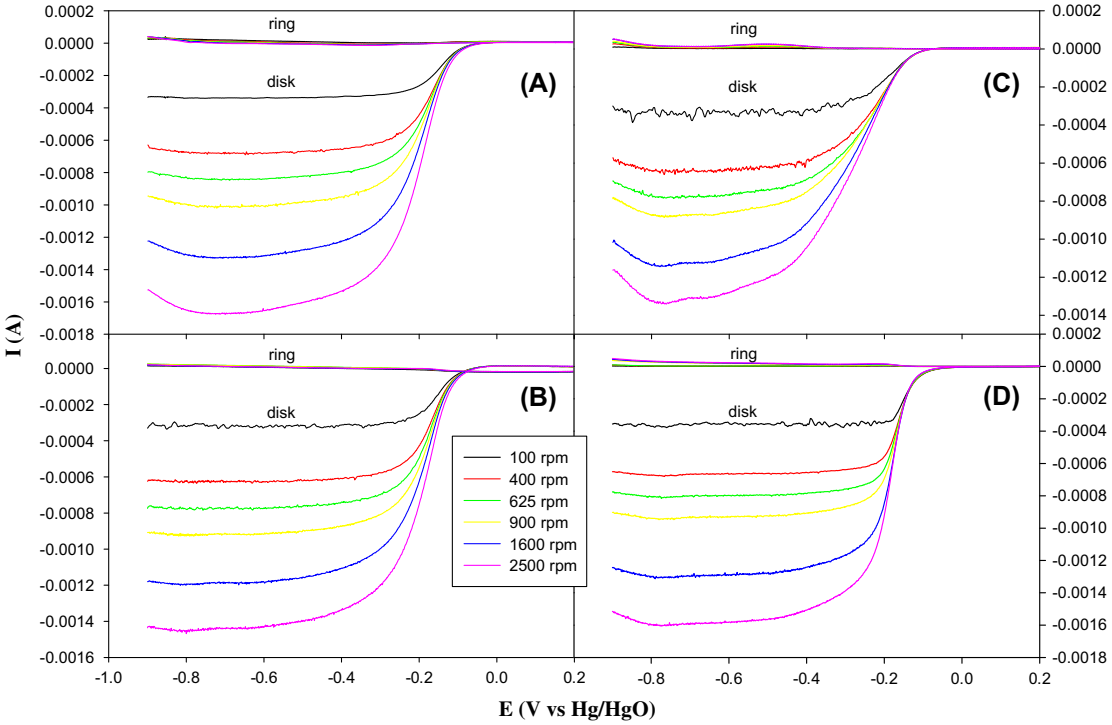

Fig. 8. RRDE voltammograms of a gold ring – glassy-carbon disk electrode modified with (A) PtHC10, (B) PtEPA, (C) PtBPA and (D) commercial Pt/C nanoparticles in an oxygen-saturated 0.1 M NaOH solution. Electrode rotation rates are specified in the figure legends. Pt loadings were 2.44 μg (PtHC10), 1.90 μg (PtEPA), 1.90 μg (PtBPA), and 2.00 μg (Pt/C). Ring currents were collected by setting the ring potential at +0.4 V.

$$Pt(O_{2,ad}) + e^- \rightarrow Pt(O^-_{2,ad}) \quad (2)$$

where oxygen is adsorbed onto the Pt surface in a linear or bridge-bonded configuration, involving both electron donation from the filled O_2 orbitals to the empty orbitals of Pt surface atoms by σ overlap, as well as back bonding interactions from the Pt filled d orbitals to the empty O_2 antibonding orbitals (π^*). Thus, it can be seen that an increase of the Pt d vacancy would facilitate electron donation from O_2 to Pt, leading to enhanced bonding interactions between Pt and O_2 and concurrently decreasing bonding order of

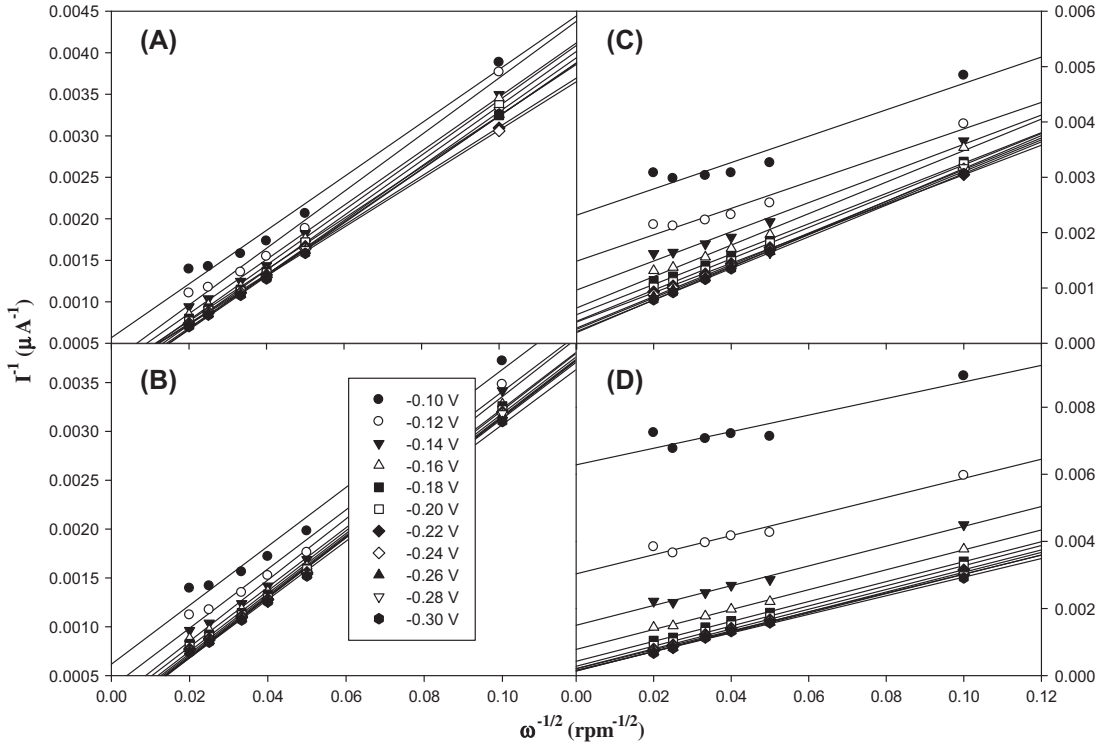

Fig. 9. Koutecky–Levich plots of (A) PtHC10, (B) PtEPA, (C) Pt-BPA and (D) commercial Pt/C nanoparticles in oxygen reduction in 0.1 M NaOH solution. Symbols are experimental data acquired from Fig. 8 and lines are the corresponding linear regressions.

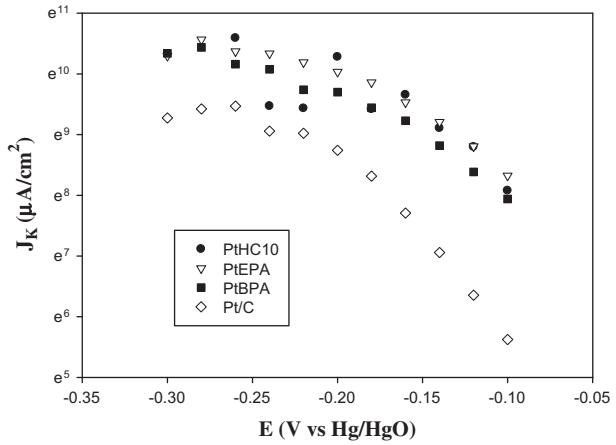

Fig. 10. Variation of the kinetic current density (J_K) with electrode potential at different nanoparticle catalysts in oxygen reduction. Symbols are experimental data obtained from the intercepts in Fig. 9 and normalized to the effective electrochemical surface areas estimated from Fig. 7.

O—O. Consequently, oxygen reduction is enhanced. Of the three nanoparticles under study above, extensive spilling of the Pt core electrons to the ligand shells is anticipated to occur because of the conjugated metal–ligand interfacial bonding interactions, and this intraparticle charge delocalization is more effective for the PtEPA and PtBPA nanoparticles than for the PtHC10 nanoparticles, as manifested in spectroscopic measurements presented above. Therefore, the effective electron density within the PtEPA and PtBPA nanoparticles is anticipated to be even somewhat lower than that of PtHC10, leading to enhanced bonding adsorption between O_2 and Pt and eventual oxygen reduction activity. However, the less effective desorption of BPA ligands from the Pt nanoparticles rendered it difficult for O_2 and electrolyte counter ions to access the Pt surface and hence compromised the electrocatalytic activity. Consequently, within the present experimental context, PtEPA represented the optimal conditions for oxygen electroreduction by virtue of the extensive intraparticle charge delocalization and relative ease of partial ligand desorption from the nanoparticle surface.

4. Conclusion

Stable platinum nanoparticles were prepared by thermolytic reduction of H_2PtCl_4 followed by the self-assembly of acetylene derivatives onto the bare Pt colloid surface. TEM measurements showed the average core diameter of the nanoparticles was 2.85 ± 0.62 nm. FTIR measurements confirmed the bonding interactions of the acetylene ligands onto the Pt surface with the breaking of the ≡C—H bond and the formation of $Pt_{surface}$—H and $Pt_{surface}$—C≡ at the metal–ligand interface, as manifested by the disappearance of the ≡C—H vibrational stretches and the marked redshift of the C≡C vibrational band. With the conjugated metal–ligand interfacial bonding interactions, extended conjugation occurred between the particle-bound triple bonds, leading to the emergence of unique photoluminescence properties of the nanoparticles. Additionally, electronic conductivity measurements showed that for the nanoparticles stabilized by 1-alkynes or 4-ethylphenylacetylene, the temperature dependence of the ensemble conductivity exhibited semiconducting characters whereas for the 4-tert-butylphenylacetylene-capped nanoparticles, metallic behaviors were observed instead. This discrepancy was accounted for by the reduced metal–ligand contact resistance and extensive spilling of core electrons into the organic protecting matrix. Furthermore, the acetylene-capped nanoparticles showed interesting electrocatalytic activity in oxygen reduction. On the basis of the onset potential and kinetic current density, all three nanoparticles exhibited improved performance as compared to naked commercial Pt/C catalysts; and among the series, 4-ethylphenylacetylene-capped nanoparticles exhibited the best electrocatalytic performance. This was accounted for by the deliberate manipulation of the Pt core electronic structure that impacted the bonding interactions with adsorbed oxygen and accessibility of the Pt surface by electrolyte counterions. The results presented herein further demonstrate the effectiveness of surface chemical functionalization in the manipulation and optimization of nanoparticle electrocatalytic activity in fuel cell electrochemistry.

Acknowledgments

This work was supported, in part, by the National Science Foundation (CHE – 1012256 and DMR – 0804049) and the ACS Petroleum Research Fund (49137 – ND10). TEM studies were carried out at the National Center for Electron Microscopy, Lawrence Berkeley National Laboratory as part of a user project.

References

[1] S.W. Chen, Electroanalytical Chemistry, in: A.J. Bard, C.G. Zoski (Eds.), vol. 23, 2010, pp. 171.
[2] D. Ghosh, S.W. Chen, Journal of Materials Chemistry 18 (2008) 755.
[3] D. Ghosh, S. Pradhan, W. Chen, S.W. Chen, Chemistry of Materials 20 (2008) 1248.
[4] W. Chen, S.W. Chen, F.Z. Ding, H.B. Wang, L.E. Brown, J.P. Konopelski, Journal of the American Chemical Society 130 (2008) 12156.
[5] W. Chen, L.E. Brown, J.P. Konopelski, S.W. Chen, Chemical Physics Letters 471 (2009) 283.
[6] W. Chen, N.B. Zuckerman, J.W. Lewis, J.P. Konopelski, S.W. Chen, Journal of Physical Chemistry C 113 (2009) 16988.
[7] W. Chen, N.B. Zuckerman, X.W. Kang, D. Ghosh, J.P. Konopelski, S.W. Chen, Journal of Physical Chemistry C 114 (2010) 18146.
[8] W. Chen, N.B. Zuckerman, J.P. Konopelski, S.W. Chen, Analytical Chemistry 82 (2010) 461.
[9] W. Chen, S. Pradhan, S.W. Chen, Nanoscale 3 (2011) 2294.
[10] X.W. Kang, N.B. Zuckerman, J.P. Konopelski, S.W. Chen, Journal of the American Chemical Society 134 (2012) 1412.
[11] Z.Y. Zhou, X.W. Kang, Y. Song, S.W. Chen, Chemical Communications 47 (2011) 6075.
[12] Z.Y. Zhou, J. Ren, X.W. Kang, Y. Song, S.G. Sun, S.W. Chen, Physical Chemistry Chemical Physics 14 (2012) 1412.
[13] Z.Y. Zhou, X.W. Kang, Y. Song, S.W. Chen, Chemical Communications 48 (2012) 3391.
[14] E.L. Muetterties, M.C. Tsai, S.R. Kelemen, Proceedings of the National Academy of Sciences of the United States of America-Physical Sciences 78 (1981) 6571.
[15] D.H. Whiffen, Spectrochimica Acta 7 (1955) 253.
[16] X.W. Kang, N.B. Zuckerman, J.P. Konopelski, S.W. Chen, Angewandte Chemie-International Edition 49 (2010) 9496.
[17] H. Feilchenfeld, M.J. Weaver, Journal of Physical Chemistry 93 (1989) 4276.
[18] J.A. Creighton, D.G. Eadon, Journal of the Chemical Society-Faraday Transactions 87 (1991) 3881.
[19] H.K. Black, D.H.S. Horn, B.C.L. Weedon, Journal of the Chemical Society 1704 (1954).
[20] E. Glimsdal, M. Carlsson, T. Kindahl, M. Lindgren, C. Lopes, B. Eliasson, Journal of Physical Chemistry A 114 (2010) 3431.
[21] S.W. Chen, in: Y.H. Lin, H.S. Nalwa (Eds.), Handbook of electrochemical nanotechnology, vol. 1, American Scientific Publishers, Los Angeles, California, CA, 2009, p. 201.
[22] D.R. Lide, CRC Handbook of Chemistry and Physics : a Ready-Reference Book of Chemical and Physical Data, CRC Press, Boca Raton, Fla., 2004.
[23] D. Mann, A. Javey, J. Kong, Q. Wang, H.J. Dai, Nano Letters 3 (2003) 1541.
[24] P. Tarakeshwar, D.M. Kim, Journal of Physical Chemistry B 109 (2005) 7601.
[25] Y. Woo, G.S. Duesberg, S. Roth, Nanotechnology 18 (2007) 095203.
[26] S. Pradhan, D. Ghosh, L.P. Xu, S.W. Chen, Journal of the American Chemical Society 129 (2007) 10622.
[27] X.J. Raj, N. Rajendran, International Journal of Electrochemical Science 6 (2011) 348.
[28] J. Hankache, O.S. Wenger, Physical Chemistry Chemical Physics 14 (2012) 2685.
[29] A.J. Bard, L.R. Faulkner, Electrochemical Methods: Fundamentals and Applications, John Wiley, New York, 2001.
[30] W. Chen, J.M. Kim, S.H. Sun, S.W. Chen, Journal of Physical Chemistry C 112 (2008) 3891.
[31] U.A. Paulus, A. Wokaun, G.G. Scherer, T.J. Schmidt, V. Stamenkovic, N.M. Markovic, P.N. Ross, Electrochimica Acta 47 (2002) 3787.
[32] T. Toda, H. Igarashi, H. Uchida, M. Watanabe, Journal of the Electrochemical Society 146 (1999) 3750.